Radiology: Artificial Intelligence

ORIGINAL RESEARCH

Adnexal Lesion Discrimination Using Deep Learning Analysis of Dynamic Contrast-enhanced US Images

Manli Wu, MD[*1] • *Hong Yang, MSc*[*2] • *Ying Chen, MSc*[1] • *Shuangyu Wu, MSc*[1] • *Tianming Liang, MSc*[2] • *Man Zhang, MD*[1] • *Enze Qu, MD*[1] • *Xiaofeng Sun, BSc*[3] • *Rui Zhang, MSc*[4] • *Liang Mu, MSc*[5] • *Li Xiao, BSc*[6] • *Hong Wen, BSc*[7] • *Ruili Wang, MSc*[8] • *Tingting Liu, MSc*[9] • *Xiaotao Meng, BSc*[10] • *Manting Su, MSc*[1] • *Ying Wang, MD*[1] • *Jian Gu, MSc*[11] • *Sijia Chen, MSc*[12] • *Yaping Wang, MSc*[13] • *Qinghong Zhao, MSc*[14] • *Juan Liu, MSc*[15] • *Ping Cheng, MSc*[16] • *Ruixuan Wang, PhD*[2] • *Jianfang Hu, PhD*[**2] • *Xinling Zhang, MD*[**1]

* M.W. and H.Y. contributed equally to this work.

** J.H. and X.Z. are co–senior authors.

Author affiliations, funding, and conflicts of interest are listed at the end of this article.

See also commentary by Huber and Adams in this issue.

Radiology: Artificial Intelligence 2026; 8(1):e240786 • https://doi.org/10.1148/ryai.240786 • Content codes: AI GU

Purpose: To develop a multimodality deep learning model (Ovarian Cancer Network [OCNet]) using dynamic contrast-enhanced US images to classify adnexal lesions.

Materials and Methods: This retrospective study included patients with pathologically confirmed adnexal lesions detected at US across 14 hospitals in China between January 2018 and July 2023. Data were divided into the training set (n = 275), internal testing set (n = 57), and external testing set (n = 63). Two deep learning models ($OCNet_{manual}$ and $OCNet_{automated}$) were developed and compared with Ovarian-Adnexal Reporting and Data System (O-RADS) US and the Assessment of Different Neoplasias in the Adnexa (ADNEX) model. Diagnostic performances of radiologists with and without assistance of OCNet were also assessed.

Results: A total of 395 female patients (median age, 43 years; IQR, 31–55 years) were included (252 benign and 143 malignant lesions). $OCNet_{manual}$ and $OCNet_{automated}$ achieved an area under the receiver operating characteristic curve (AUC) of 0.94 (95% CI: 0.89, >0.99) and 0.91 (95% CI: 0.83, 0.99), respectively, outperforming O-RADS US (AUC, 0.79; 95% CI: 0.68, 0.89; P = .002 and P = .03, respectively) and the ADNEX model (AUC, 0.86; 95% CI: 0.77, 0.95; P = .04 and P = .36, respectively). Additionally, the assistance of OCNet enhanced diagnostic performance for junior radiologists, improving the average AUC from 0.86 to 0.94 and the average specificity from 52% to 73%.

Conclusion: The OCNet model achieved higher performance than O-RADS US and the ADNEX model for classifying adnexal lesions and improved the diagnostic performance of junior radiologists.

Supplemental material is available for this article.

Ovarian cancer is the eighth most common cancer among women (1–3) and the most lethal gynecologic cancer (4–6) globally, with a 5-year survival rate in China of approximately 40% (7). Precise preoperative diagnosis of ovarian cancer is essential for guiding treatment decisions, preventing unnecessary interventions, and preserving fertility (8).

US is currently the first-line recommended imaging modality for characterizing adnexal lesions (9–11). Various US-based diagnostic models, including International Ovarian Tumor Analysis, Assessment of Different Neoplasias in the Adnexa (ADNEX) model, and the American College of Radiology Ovarian-Adnexal Reporting and Data System (O-RADS) US risk system, have been implemented in recent years (9). The O-RADS US system was introduced in 2019 to standardize ovarian lesion risk assessment and management (12–14). Despite its high sensitivity, O-RADS US faces limitations with relatively low specificity in accurately differentiating between solid-appearing blood clots, debris, and solid tissue within tumors (14,15). Patients with O-RADS category 4 and 5 lesions need referral to a specialist consultation or further examination.

MRI serves as a useful secondary tool for O-RADS categories 4 and 5 adnexal lesions (9). MRI offers high-resolution (0.5–1.0 mm) images in classifying adnexal lesions. However, in regions of Asia where clinical resources are often limited, MRI is not always accessible (9). Acquiring MRI data is not only time-consuming and costly but also poses challenges for patients who have claustrophobia or those with implanted medical devices. Contrast-enhanced US (CEUS) may serve as an alternative secondary examination imaging tool. Compared with MRI, CEUS is a more cost-effective option for further characterizing adnexal lesions (16–18), particularly for those lesions containing solid components (18,19). Yet CEUS remains associated with specific shared challenges, such as its high dependence on experience. A typical CEUS video provides detailed perfusion patterns of various adnexal lesions, containing rich, valuable information for diagnosis. However, to date, there are no current guidelines on how to interpret CEUS images of adnexal lesions to assist in diagnosis. This lack of guidelines poses a challenge for US radiologists who are not well versed in the gynecologic application of the CEUS technique.

The rapid development of artificial intelligence (AI)–based deep learning (DL) is expected to address these limitations. However, most existing models rely on static images or single modalities, failing to capture the dynamic and multisource nature of

Abbreviations

ADNEX = Assessment of Different Neoplasias in the Adnexa, AI = artificial intelligence, AUC = area under the receiver operating characteristic curve, CA-125 = cancer antigen 125, CEUS = contrast-enhanced US, DL = deep learning, OCNet = Ovarian Cancer Network, O-RADS = Ovarian-Adnexal Reporting and Data System

Summary

A multimodal deep learning model integrating contrast-enhanced US images achieved higher performance than Ovarian-Adnexal Reporting and Data System US and the Assessment of Different Neoplasias in the Adnexa model for classifying adnexal lesions and improved the diagnostic performance of junior radiologists.

Key Points

- Deep learning models integrating contrast-enhanced US images named Ovarian Cancer Network (OCNet), including $OCNet_{manual}$ (area under the receiver operating characteristic curve [AUC], 0.94) and $OCNet_{automated}$ (AUC, 0.91), outperformed Ovarian-Adnexal Reporting and Data System US (AUC, 0.79; $P = .002$ and $P = .03$, respectively) and the Assessment of Different Neoplasias in the Adnexa model (AUC, 0.86; $P = .04$ and $P = .36$, respectively) in classifying adnexal lesions.
- Assistance by the OCNet model improved junior radiologists' specificity from 52% to 73% without reducing sensitivity.

Keywords

Adnexal Lesion, Deep Learning, Contrast-enhanced US, Multimodal

CEUS data (20). CEUS interpretation inherently requires precise temporal modeling. Furthermore, synergistic information from concurrent imaging modalities, such as B-mode or Doppler imaging, is often neglected in existing approaches.

In this study, we propose a multimodal DL model, Ovarian Cancer Network (OCNet), using dynamic CEUS images as a triage tool for the automatic diagnosis of adnexal lesions. We evaluated the performance of OCNet compared with O-RADS US and the ADNEX model and assessed its value in assisting radiologists.

Materials and Methods

Study Design and Patients

This retrospective study included patients with US-detected adnexal lesions from 14 hospitals in China between January 2018 and July 2023. All patients underwent preoperative CEUS examinations at least 120 days before surgery (21). Data were divided into training and internal testing sets from 11 hospitals and an external testing set from three hospitals. Ethical approval was obtained from the Third Affiliated Hospital of Sun Yat-Sen University, and the requirement for informed consent was waived due to the study's retrospective nature. Patients with a history of ovarian cancer, those pregnant during examination, and those without final pathologic results were excluded from the study. Pathologic examination served as the reference standard.

Data on baseline characteristics, including age, cancer antigen 125 (CA-125) levels, menopausal status, and pathologic outcomes, were collected from the hospital database. Postmenopausal status was defined as age over 50 years with a history of hysterectomy or 12 consecutive months of amenorrhea.

For bilateral adnexal lesions, the lesion with the most complex US morphology was selected for analysis. If the US morphology of both masses was similar, the largest mass was selected for analysis. All images were anonymized and assigned unique numerical identifiers. Figure 1 outlines the study workflow.

Imaging Protocol

Preoperative pelvic US, including both unenhanced US and CEUS, were conducted using three systems: Philips EPIQ 7 (Philips Healthcare), Mindray Nuewa R9/Resona 7 (Mindray), and GE LOGIQ E9 (GE HealthCare). Experienced radiologists with more than 5 years of experience in gynecologic US performed these examinations without access to patients' clinical information. For CEUS, 1.5 mL (for transabdominal protocol) or 2.4 mL (for transvaginal protocol) of contrast agent (SonoVue; Bracco) was injected, followed by a 5-mL saline flush, with recording starting at injection to maintain timing consistency. A 90-second video was captured using a stationary probe, primarily transvaginally, but transabdominally for lesions exceeding 6 cm.

O-RADS US and ADNEX Assessment

To maintain quality control, two senior radiologists (M.Z. and E.Q.) with more than 5 years of experience in gynecologic US independently reviewed all images without access to patients' clinical or pathologic data. Lesions in the external testing set were evaluated using the updated 2022 O-RADS US lexicon, with each lesion assigned an O-RADS category and assessed via the ADNEX model for malignancy probability. Any assessment discrepancies were resolved through discussion.

The ADNEX model (22) is based on nine predictor variables, including three clinical variables and six US variables: type of center, patient age, CA-125 level, maximum diameter of the lesion, proportion of solid tissue, number of papillary projections, presence of more than 10 cyst locules, presence of acoustic shadows, and presence of ascites.

CEUS Image Preprocessing

The extraction of CEUS key frames was primarily conducted via manual frame extraction.

For manual extraction, MicroDicom Viewer software (version 3.4.7; MicroDicom) was used to convert CEUS videos into static frames. A radiologist (M.W., with 5 years of experience in gynecologic US) drew a region of interest that outlined the lesion border on the CEUS video to generate a time-intensity curve, which was generated either on the US machine or offline. Using the time-intensity curve, six representative frames (T1, beginning of enhancement; T2, 10 seconds before peak enhancement; T3, 5 seconds before peak enhancement; T4, time of peak enhancement; T5, 10 seconds after peak enhancement; T6, 20 seconds after peak enhancement) were extracted from the CEUS video (Fig 2).

Automated extraction of CEUS key frames was also investigated in the study. The approach is outlined in Figure S1.

Development of Multimodality OCNet Model

The study developed two OCNet models, $OCNet_{manual}$ and $OCNet_{automated}$. Both models incorporated four modalities: CEUS

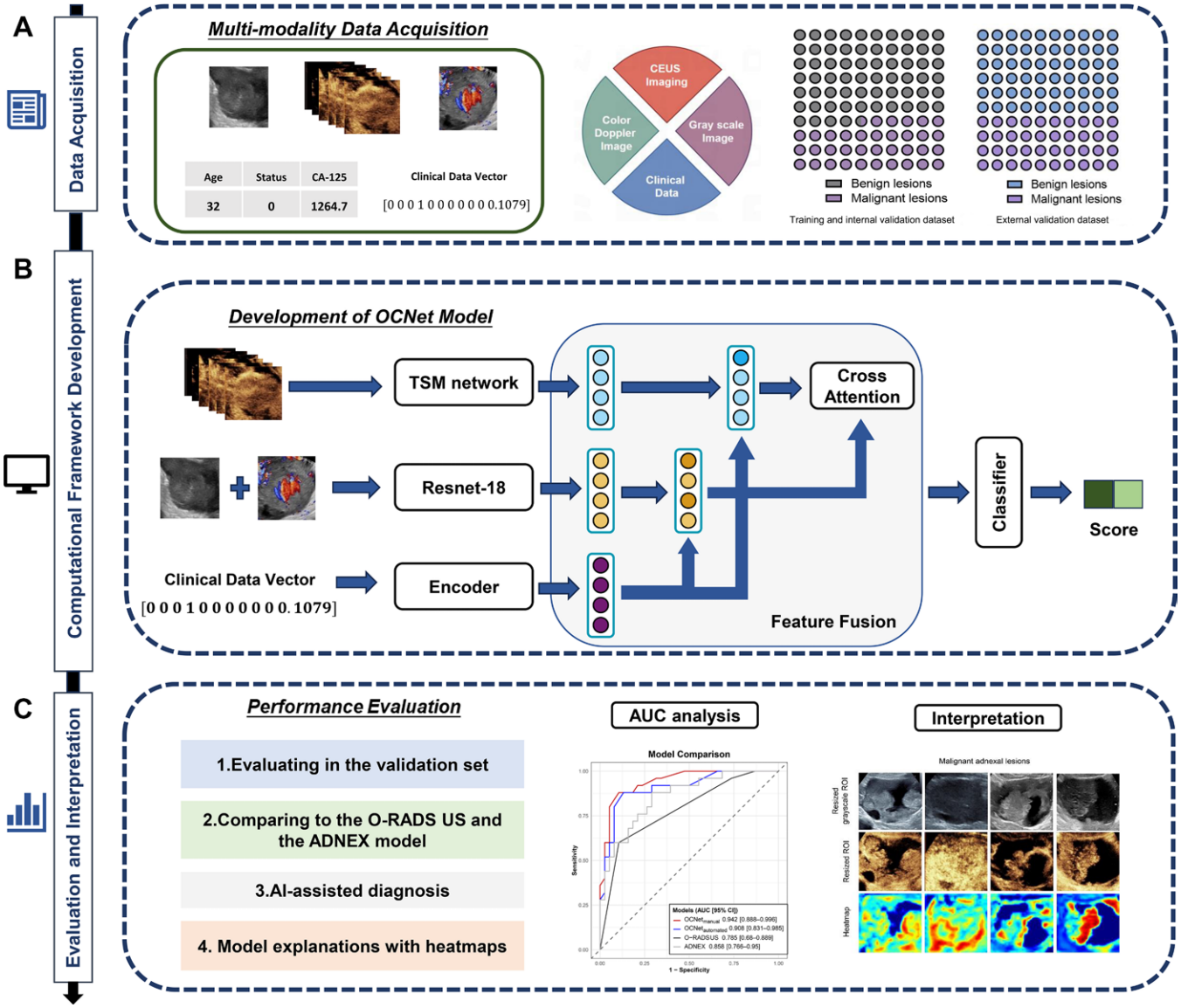

Figure 1: Study workflow. **(A)** Data acquisition of multimodality Ovarian Cancer Network (OCNet) model. **(B)** Development of OCNet model. **(C)** Performance evaluation and interpretation of OCNet model. ADNEX = Assessment of Different Neoplasias in the Adnexa, AI = artificial intelligence, AUC = area under the receiver operating characteristic curve, CA-125 = cancer antigen 125, CEUS = contrast-enhanced US, O-RADS = Ovarian-Adnexal Reporting and Data System, ROI = region of interest.

images, color Doppler images, grayscale US images, and clinical data. Visual data were standardized to a 256 × 256 resolution. Clinical data comprised age, CA-125 level, and menopausal status, with age grouped into 10-year intervals using one-hot encoding and CA-125 levels normalized.

Figure 3 illustrates the overall framework of OCNet, which consists of three stages: feature extraction, multimodal fusion, and cognitive reasoning. In the first stage, a multimodal feature extractor gathered features from different data sources, including CEUS images, color Doppler images, grayscale US images, and clinical text data. This extractor included three branches: a dynamic temporal shift module for extracting dynamic visual information from CEUS images, a static ResNet18 for static visual information from color Doppler and grayscale US images, and an attribute encoder with vector quantization for clinical attributes. The temporal shift module enhances temporal modeling by shifting some channels along the temporal dimension before spatial convolutions, without requiring computation. Channels were divided into three groups: one shifting forward, one shifting backward, and one remaining static. For a feature map, shifts were precisely defined per group. The temporal receptive field was set to six, representing six key frames or segments, with a shift stride of one due to the limited segments. Optimization was achieved using the AdamW optimizer and LambdaLR scheduler, with label smoothing at 0.05 to reduce overfitting and a dropout rate of 0.7. During testing, we followed the same procedure as in the training phase.

In the second stage, a multimodal fusion module was developed to combine features from different branches. Initially, fully connected layers projected the features from the first stage into a shared space, with each feature handled by a separate fully connected layer. Clinical features then guided visual features using a Hadamard product, enabling the clinical features to activate key regions within the visual features. The enhanced CEUS dynamic features were fused with other static image features using a cross-attention mechanism, in which dynamic visual features served as the query and static visual features as the key and value. Static image features were also integrated through element-wise

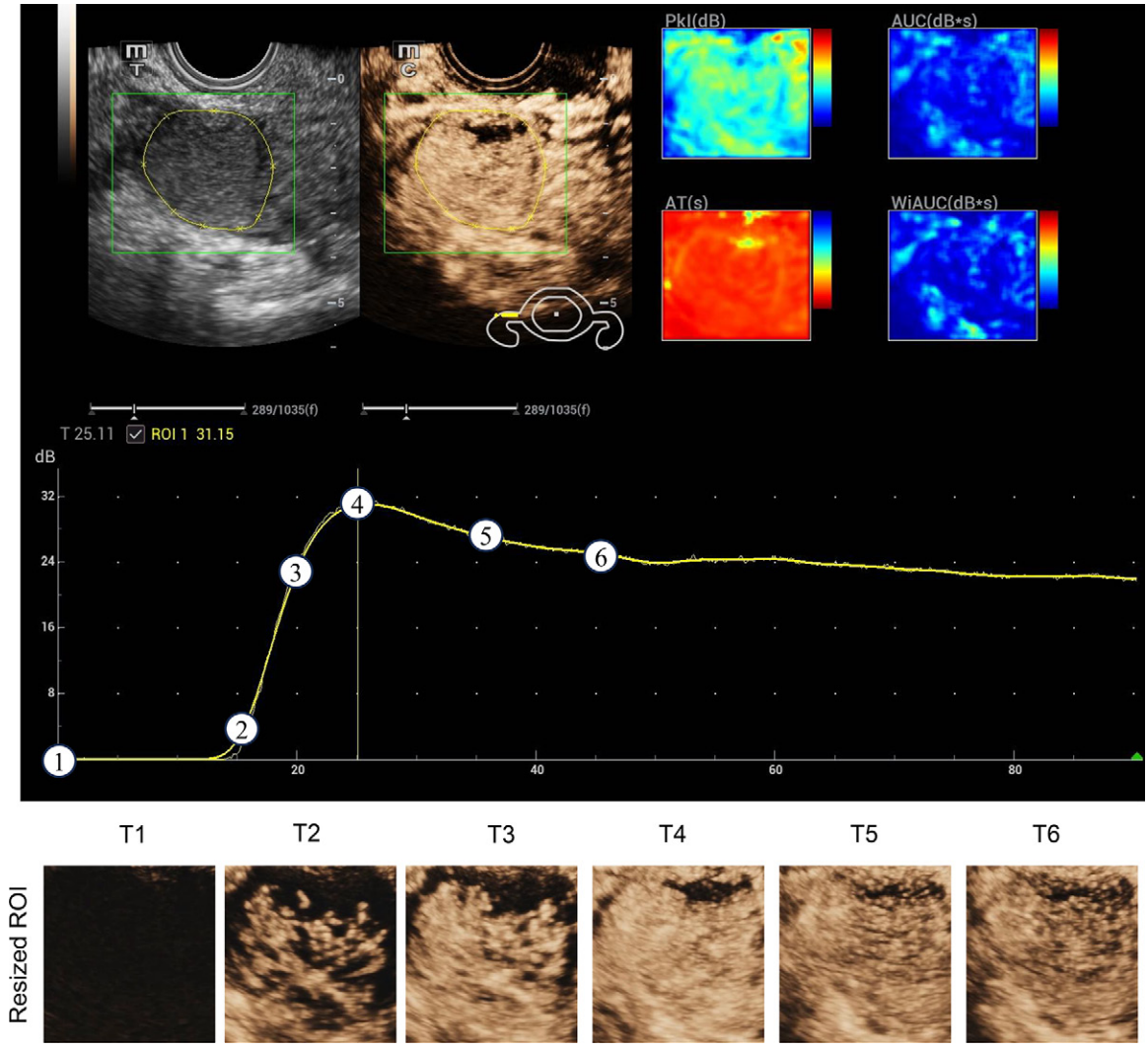

Figure 2: Data preprocessing for manual extraction of contrast-enhanced US (CEUS) images. Based on the time-intensity curve of the ovarian lesion (T1, beginning of enhancement; T2, 10 seconds before peak enhancement; T3, 5 seconds before peak enhancement; T4, time of peak enhancement; T5, 10 seconds after peak enhancement; T6, 20 seconds after peak enhancement), a maximum cross-section static image and six representative frames were extracted from CEUS data. ROI = region of interest.

addition. Ultimately, all fused features were input into the classifier for prediction.

In the third stage, a multibranch cognition block was created for advanced recognition, functioning in two steps. Ultimately, a mean pooling operator combined all initial recognition results for a more reliable outcome.

Our model was developed using PyTorch (version 2.0.1; Linux Foundation) and trained on NVIDIA GeForce RTX 3090 graphics processing units. As shown in Figure 3, all DL networks were trained from scratch in an end-to-end manner. We used AdamW as the optimizer, with a learning rate of 0.001, a weight decay of 0.0001, and a batch size of 16, following best practices.

The LambdaLR scheduler from torch.optim.lr_scheduler was used with the AdamW optimizer, adjusting the learning rate by multiplying it by 0.995 each epoch, resulting in a power function decay.

To interpret the OCNet's predictions, heatmaps were generated using gradient-weighted class activation mapping.

The performance of OCNet's multibranch fusion architecture and its capacity to integrate information from multiple modalities was also evaluated. In our comparative analysis, we used standard fusion methods prevalent in the field of multimodal research and focused on the comparison of fusion strategies for three types of imaging data after integrating the features of clinical data.

AI-assisted Diagnosis

In the external testing set, AI-assisted diagnosis was used to evaluate 63 lesions for malignancy.

The assessment involved five senior readers (with more than 5 years of experience in gynecologic US) and five junior readers (with 1 or 2 years of experience in gynecologic US), all blinded to each other's evaluations and without access to pathologic results. All readers were fixed and uniquely selected. The modified CEUS O-RADS US score (Table S1) was used for assessment. Based on established criteria (16), the O-RADS category was upgraded for a CEUS score of 4 or more, downgraded for a score of 2 or less, and remained unchanged for a score of 3.

The AI-assisted diagnostic decision-making process was made by averaging the probabilities assigned by the model and the readers.

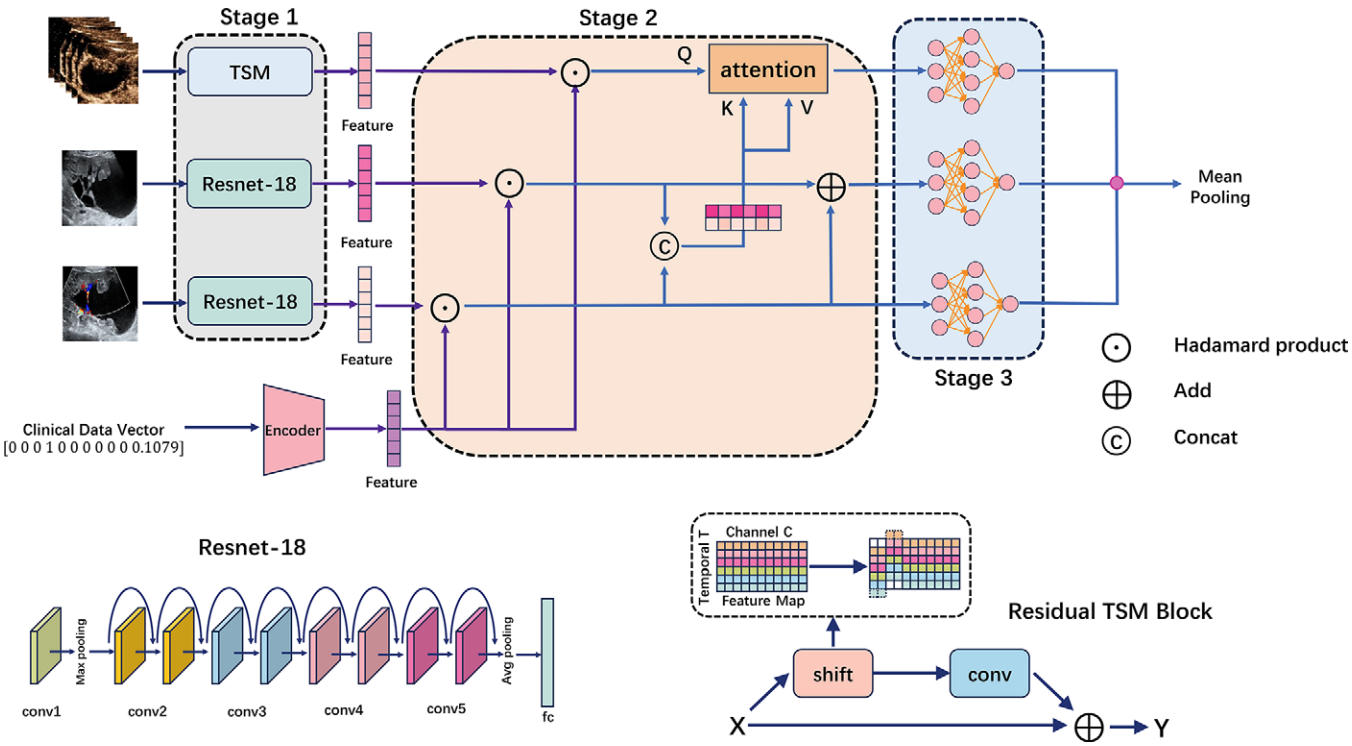

Figure 3: Flowchart and architectural framework of the proposed Ovarian Cancer Network model. TSM = temporal shift module.

Statistical Analysis

Categorical variables are described as numbers (percentages) and were compared with the χ^2 test. Continuous variables are expressed as medians (IQRs) and were analyzed using the Mann-Whitney *U* test. The model's diagnostic performance was evaluated with AUC (95% CIs), with AUC comparisons tested via DeLong statistics. Decision curve and calibration curve analysis were also conducted. A 10% cutoff for ADNEX indicated malignancy, with O-RADS US 4 and 5 also considered malignant. AI model cutoffs were set based on a negative likelihood ratio near 0.10, with $OCNet_{manual}$ and $OCNet_{automated}$ cutoffs at 0.251 and 0.181, respectively. Therefore, we chose a cutoff of 0.200 for both models. Sensitivity, specificity, and predictive values with 95% CIs were presented, and sensitivity and specificity were compared using the McNemar test. A Bayesian logistic mixed-effects model was performed to evaluate intraclass correlation coefficients to assess agreement across readers. All analyses were conducted using R software (version 4.4.3; R Foundation) and Python (version 3.7.15; Python Software Foundation).

$P < .05$ indicated a significant difference. For statistical considerations, a borderline ovarian tumor was considered malignant.

Code Availability

The code base for training the DL models used in this study is available at *https://github.com/1325116124/DL-Adnexal-Lesions/tree/master*.

Results

Dataset Characteristics

A total of 395 female patients (median age, 43 years [IQR, 31–55 years]) were included (252 benign and 143 malignant lesions). Data were divided into the training set (n = 275), internal testing set (n = 57), and external testing set (n = 63). Table 1 provides a detailed summary of the baseline characteristics of the training and testing sets. The malignancy rate was 34.5% (95 of 275), 40.4% (23 of 57), and 39.7% (25 of 63) in the training set, internal testing set, and external testing set, respectively.

OCNet, O-RADS US, and the ADNEX Model for Classifying Adnexal Lesions

As presented in Table 2, $OCNet_{manual}$ and $OCNet_{automated}$ yielded high classification performance in distinguishing malignant from benign adnexal lesions, both in the internal (AUC, 0.99 [95% CI: 0.97, >0.99] vs AUC, 0.99 [95% CI: 0.96, >0.99]) and external testing set (AUC, 0.94 [95% CI: 0.89, >0.99] vs AUC, 0.91 [95% CI: 0.83, 0.99]). We found no evidence of a difference in the AUCs between $OCNet_{manual}$ and $OCNet_{automated}$ (P = .79 and P = .28 in the internal and external testing sets, respectively).

Figure 4 shows the AUC comparisons between $OCNet_{manual}$, $OCNet_{automated}$, O-RADS US, and the ADNEX model in characterizing adnexal lesions in the external testing set. Both $OCNet_{manual}$ and $OCNet_{automated}$ demonstrated higher performance relative to O-RADS US (AUC, 0.79; 95% CI: 0.68, 0.89; P = .002 and P = .03, respectively). $OCNet_{manual}$ and $OCNet_{automated}$ also presented improved specificity versus O-RADS US (87% vs 26%; $P < .001$ and 84% vs 26%; $P < .001$, respectively). $OCNet_{manual}$ presented improved diagnostic performance compared with the ADNEX model (AUC, 0.86; 95% CI: 0.77, 0.95; P = .04). There was no evidence of differences in the AUCs between $OCNet_{automated}$ and the ADNEX model (P = .36). However, higher specificities were observed in $OCNet_{manual}$ and $OCNet_{automated}$ compared with the

Table 1: Baseline Characteristics of Each Dataset

Characteristic	Training Set (*n* = 275)	Internal Testing Set (*n* = 57)	External Testing Set (*n* = 63)
Menopausal status			
Premenopausal	194 (70.5)	29 (50.9)	39 (61.9)
Menopausal	81 (29.5)	28 (49.1)	24 (38.1)
Age (y)	39.0 (29.0–54.0)	47.0 (33.0–57.0)	48.0 (35.5–57.5)
Cancer antigen 125 (U/mL)*	28.8 (18.2–102.9)	47.2 (17.8–239.4)	20.8 (20.0–139.9)
Pathology			
Benign lesions	180 (65.5)	34 (59.6)	38 (60.3)
Ovarian theca-fibroma	20 (7.3)	4 (7.0)	5 (7.9)
Mature teratoma	38 (13.8)	6 (10.5)	14 (22.2)
Cystadenoma	46 (16.7)	11 (19.3)	7 (11.1)
Cystadenofibroma	2 (0.7)	0	0
Endometrioma	48 (17.5)	6 (10.5)	7 (11.1)
Pelvic abscess	5 (1.8)	0	1 (1.6)
Pelvic inflammatory disease	8 (2.9)	0	0
Simple cyst	10 (3.6)	6 (10.5)	2 (3.2)
Functional cyst	2 (0.7)	1 (1.8)	0
Corpus luteum	1 (0.4)	0	0
Other benign lesions	0	0	2 (3.2)
Malignant lesions	95 (34.5)	23 (40.4)	25 (39.7)
Borderline lesions	23 (8.4)	3 (5.3)	6 (9.5)
Serous cystadenocarcinoma	43 (15.6)	11 (19.3)	6 (9.5)
Mucinous cystadenocarcinoma	0	0	1 (1.6)
Adenocarcinoma	7 (2.5)	2 (3.5)	4 (6.3)
Endometrioid carcinoma	3 (1.1)	1 (1.8)	0
Germ cell tumor	4 (1.5)	0	1 (1.6)
Clear cell tumor	4 (1.5)	3 (5.3)	2 (3.2)
Metastatic cancer	7 (2.5)	0	2 (3.2)
Other malignant lesions	4 (1.5)	3 (5.3)	3 (4.8)

Note.—Continuous variables are medians with IQRs in parentheses; categorical variables are numbers with percentage in parentheses. One lesion per patient.
* To convert to kilounits per liter, multiply by one.

Table 2: Diagnostic Performance of $OCNet_{manual}$ and $OCNet_{automated}$ for Adnexal Lesions

Variable	AUC*	Sensitivity*	Specificity*	PPV	NPV
Internal testing set†					
$OCNet_{manual}$	0.99 (0.97, >0.99)	91 (72, 99)	85 (69, 95)	81 (61, 93)	94 (79, 99)
$OCNet_{automated}$	0.99 (0.96, >0.99)	91 (72, 99)	91 (76, 98)	88 (68, 97)	94 (80, 99)
External testing set†					
$OCNet_{manual}$	0.94 (0.89, >0.99)	88 (69, 98)	87 (72, 96)	82 (62, 94)	92 (78, 98)
$OCNet_{automated}$	0.91 (0.83, 0.99)	88 (69, 98)	84 (69, 94)	79 (59, 92)	91 (77, 98)

Note.—Data in parentheses are 95% CIs. Sensitivity, specificity, positive predictive value (PPV), and negative predictive value (NPV) are percentages. AUC = area under the receiver operating characteristic curve, OCNet = Ovarian Cancer Network.
* All comparisons were not significantly different ($P > .05$).
† Cutoffs for $OCNet_{manual}$ and $OCNet_{automated}$ were 0.200 for diagnosing adnexal malignancy.

ADNEX model in assessing adnexal lesions (87% vs 32%; $P < .001$ and 84% vs 32%; $P < .001$, respectively).

Table S2 presents the adjusted positive predictive values, negative predictive values, and Brier scores for the OCNet model using a prevalence of 10%. The decision curve and model calibration analysis are illustrated in Figures S2 and S3.

Comparison of Performance between OCNet and Radiologists

In the external testing set, the senior radiologists obtained an average AUC of 0.93, as depicted in Table 3. When comparing the performance between OCNet and radiologists, both $OCNet_{manual}$ and $OCNet_{automated}$ showed a markedly higher AUC and specificity compared with the junior radiologists in the

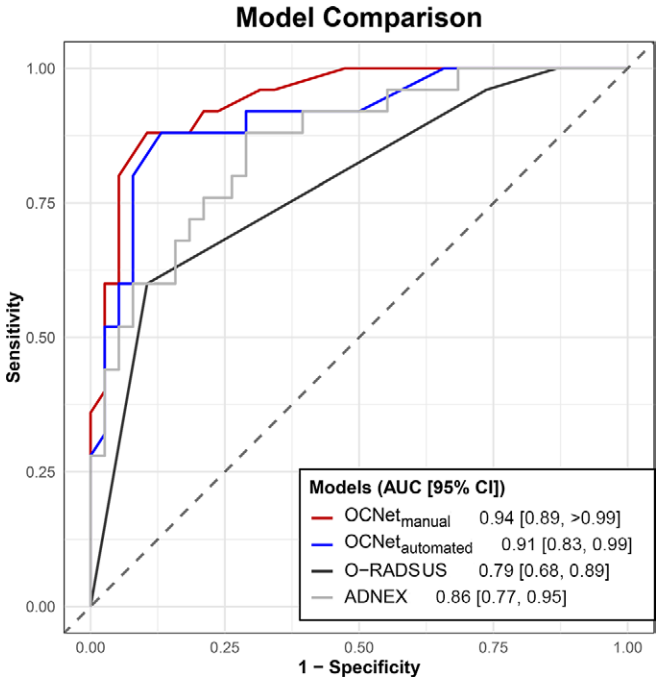

Figure 4: Graph of performance comparison of area under the receiver operating characteristic curve (AUC) values among the proposed Ovarian Cancer Network (OCNet), Ovarian-Adnexal Reporting and Data System (O-RADS) US, and Assessment of Different Neoplasias in the Adnexa (ADNEX) model.

external testing dataset. However, we found no evidence of a difference in AUCs between OCNet and the senior readers in assessing adnexal lesions.

AI-assisted Diagnosis

The impact of AI assistance on diagnostic performance between senior and junior radiologists is presented in Table 3. The average AUC for the junior readers was improved from 0.86 to 0.94 when using OCNet in the external testing dataset. Specifically, the average specificities for the junior readers increased from 52% to 73% with the aid of OCNet. With the assistance of OCNet, the junior radiologists achieved diagnostic performance comparable to that of the senior radiologists without AI assistance. For the senior readers, assistance of OCNet brought only small benefits and did not yield any differences in diagnostic performance. The logistic mixed-effects model showed that the intraclass correlation coefficient for experience level was 0.162, indicating 16.2% of variance attributable to experience level. The corresponding intraclass correlation coefficient between radiologists was 0.0025, indicating only 0.25% of variance due to individual differences. This finding indicates that diagnostic performance variability was primarily driven by experience level, not by individual reader differences.

Interpretation of Model Prediction

As shown in Figure 5, for malignant lesions, OCNet focused on the tumor area, while for benign lesions, it focused on the lesion boundaries. Figure S4 demonstrates the relationship between the temporal analysis of CEUS sequences and heatmap visualization.

Details of Lesions Misclassified by OCNet

Table 4 details the lesions misclassified by OCNet. OCNet$_{manual}$ and OCNet$_{automated}$ misclassified seven (four benign, three malignant) and nine (six benign, three malignant) lesions, respectively. As illustrated in Figure 6, all target regions of the heatmaps identified by OCNet$_{manual}$ were consistent with the senior reader's findings. Among its misclassified cases, four benign lesions exhibited malignant features on CEUS, potentially leading to model error. Conversely, two of the three misclassified malignant lesions displayed malignant characteristics on CEUS that the model failed to identify; the third (ID: 2-1-060) exhibited benign enhancement patterns, making correct classification challenging.

Discussion

The use of CEUS for assessing adnexal pathologies is gaining interest. Integrating CEUS into O-RADS US classifications improves lesion differentiation (18,19), offering a viable alternative where MRI is unavailable. However, its global adoption in gynecology remains limited by the requirement for specialized examiners. To our knowledge, this retrospective multicenter study proposed the first DL models that integrate CEUS images with high performance for classifying adnexal lesions. In the external testing test, both OCNet$_{manual}$ and OCNet$_{automated}$ models revealed high diagnostic performance, with AUCs of 0.94 (95% CI: 0.89, >0.99) and 0.91 (95% CI: 0.83, 0.99), respectively, outperforming the O-RADS US system and achieving higher specificity compared with the ADNEX model. With the assistance of OCNet, the average specificity of the junior radiologists was markedly improved from 52% to 73% without compromising sensitivity, suggesting its potential to reduce false-positive results in clinical practice.

Our OCNet model demonstrated higher diagnostic specificity for classifying adnexal lesions compared with the O-RADS US system and the ADNEX model. Unlike the study by Moro et al (23), in which the ADNEX model was nearly as effective as expert US assessment, our study shows OCNet's superior specificity. This difference may be due to our inclusion of CEUS images, which enhance diagnostic performance, and the inclusion of more complex adnexal lesions, which may lower the specificity of the ADNEX model.

In line with the findings of previous studies, our study confirmed that DL models could serve as an effective imaging tool in differentiating malignant from benign ovarian tumors (24–26). Chen et al (27) suggested that the DL algorithms using US images can achieve a high AUC of 0.93, which is comparable with expert assessments. More recently, Xiang et al (28) developed OvcaFinder by integrating image-based DL predictions, readers' assessments, and clinical parameters, with an AUC of 0.947 for assessing ovarian cancer. A noteworthy feature of our research is the integration of multimodality data, which integrated dynamic CEUS images for the first time. Additionally, our model also demonstrated robust cross-device generalization. Although being primarily trained on Mindray systems, both OCNet$_{manual}$ and OCNet$_{automated}$ maintained high AUCs on Philips (0.97 and 0.94, respectively) and GE (0.90 and 0.92, respectively) devices. These results highlight the model's strong cross-device generalization capability.

Table 3: Impact of Artificial Intelligence Assistance on Diagnostic Performance between Senior and Junior Radiologists

Variable	AUC*	Sensitivity†	Specificity‡	PPV	NPV
Junior radiologists					
Without OCNet					
Reader 1	0.87 (0.78, 0.95)	92 (74, 99)	53 (36, 69)	56 (40, 72)	91 (71, 99)
Reader 2	0.85 (0.76, 0.94)	96 (80, 100)	47 (31, 64)	55 (39, 70)	95 (74, 100)
Reader 3	0.86 (0.78, 0.94)	100 (86, 100)	50 (33, 67)	57 (41, 72)	100 (82, 100)
Reader 4	0.87 (0.80, 0.95)	100 (86, 100)	50 (33, 67)	57 (41, 72)	100 (82, 100)
Reader 5	0.86 (0.78, 0.94)	100 (86, 100)	58 (41, 74)	61 (45, 76)	100 (85, 100)
With $OCNet_{manual}$					
Reader 1	0.94 (0.88, >0.99)	92 (74, 99)	82 (66, 92)	77 (58, 90)	94 (80, 99)
Reader 2	0.94 (0.89, 0.99)	92 (74, 99)	79 (63, 90)	74 (55, 88)	94 (79, 99)
Reader 3	0.94 (0.89, >0.99)	96 (80, 100)	71 (54, 85)	69 (51, 83)	96 (82, 100)
Reader 4	0.95 (0.90, >0.99)	96 (80, 100)	79 (63, 90)	75 (57, 89)	97 (83, 100)
Reader 5	0.95 (0.90, >0.99)	100 (100, 100)	74 (57, 87)	71 (54, 85)	100 (100, 100)
With $OCNet_{automated}$					
Reader 1	0.94 (0.88, >0.99)	96 (80, 100)	74 (57, 87)	71 (53, 85)	97 (82, 100)
Reader 2	0.94 (0.88, 0.99)	100 (100, 100)	74 (57, 87)	71 (54, 85)	100 (100, 100)
Reader 3	0.95 (0.89, >0.99)	100 (100, 100)	63 (46, 78)	64 (47, 79)	100 (100, 100)
Reader 4	0.94 (0.89, >0.99)	100 (100, 100)	71 (54, 85)	69 (52, 84)	100 (100, 100)
Reader 5	0.94 (0.88, >0.99)	100 (100, 100)	68 (51, 83)	68 (50, 82)	100 (100, 100)
Senior radiologists					
Without OCNet					
Reader 6	0.93 (0.86, 0.99)	92 (74, 99)	79 (63, 90)	74 (55, 88)	94 (79, 99)
Reader 7	0.92 (0.85, 0.99)	88 (69, 98)	79 (63, 90)	73 (54, 88)	91 (76, 98)
Reader 8	0.92 (0.85, 0.99)	88 (69, 98)	79 (63, 90)	73 (54, 88)	91 (76, 98)
Reader 9	0.94 (0.88, >0.99)	92 (74, 99)	84 (69, 94)	79 (60, 92)	94 (80, 99)
Reader 10	0.93 (0.86, 0.99)	88 (69, 98)	79 (63, 90)	73 (54, 88)	91 (76, 98)
With $OCNet_{manual}$					
Reader 6	0.96 (0.92, >0.99)	96 (80, 100)	90 (75, 97)	86 (67, 96)	97 (85, 100)
Reader 7	0.96 (0.91, >0.99)	92 (74, 99)	90 (75, 97)	85 (66, 96)	94 (81, 99)
Reader 8	0.96 (0.91, >0.99)	92 (74, 99)	90 (75, 97)	85 (66, 96)	94 (81, 99)
Reader 9	0.97 (0.94, >0.99)	96 (80, 100)	92 (79, 98)	89 (71, 98)	97 (86, 100)
Reader 10	0.96 (0.92, >0.99)	92 (74, 99)	90 (75, 97)	85 (66, 96)	94 (81, 99)
With $OCNet_{automated}$					
Reader 6	0.96 (0.92, >0.99)	100 (100, 100)	87 (72, 96)	83 (65, 94)	100 (100, 100)
Reader 7	0.96 (0.91, >0.99)	84 (64, 96)	92 (79, 98)	88 (68, 97)	90 (76, 97)
Reader 8	0.95 (0.91, >0.99)	84 (64, 96)	92 (79, 98)	88 (68, 97)	90 (76, 97)
Reader 9	0.97 (0.93, >0.99)	100 (100, 100)	87 (72, 96)	83 (65, 94)	100 (100, 100)
Reader 10	0.96 (0.92, >0.99)	96 (80, 100)	84 (69, 94)	80 (61, 92)	97 (84, 100)

Note.—Data in parentheses are 95% CIs. Sensitivity, specificity, positive predictive value (PPV), and negative predictive value (NPV) are percentages. AUC = area under the receiver operating characteristic curve, OCNet = Ovarian Cancer Network.

* The assistance of $OCNet_{manual}$ and $OCNet_{automated}$ significantly improved the AUCs for junior radiologists (all $P < .05$). For senior radiologists, all comparisons were not significantly different ($P > .05$).

† For sensitivity analysis, all comparisons were not significantly different ($P > .05$).

‡ The assistance of $OCNet_{manual}$ and $OCNet_{automated}$ significantly improved the specificities for junior radiologists, except for the difference between reader 3 with $OCNet_{automated}$ and reader 3 without OCNet ($P = .07$). For senior radiologists, all comparisons for specificities were not significantly different ($P > .05$).

In our study, the $OCNet_{manual}$ model misclassified seven lesions in the external testing set. Among the four benign misdiagnoses, all were either infected endometriomas or atypical mature teratomas. These lesions exhibited features on both conventional US and CEUS that closely mimicked malignancy, thereby challenging the model and limiting its performance. To address this limitation and enhance the model's robustness for complex lesions, future work will focus on expanding the training dataset.

Our model is designed to work seamlessly with the common picture archiving and communication systems by following established protocols, such as using Digital Imaging and Communications in Medicine for image transmission and Health Level Seven for connecting with electronic health records. In practice, radiologists would first evaluate the model's heatmaps for credibility. If considered credible, radiologists can use the model's probability estimation to downgrade or

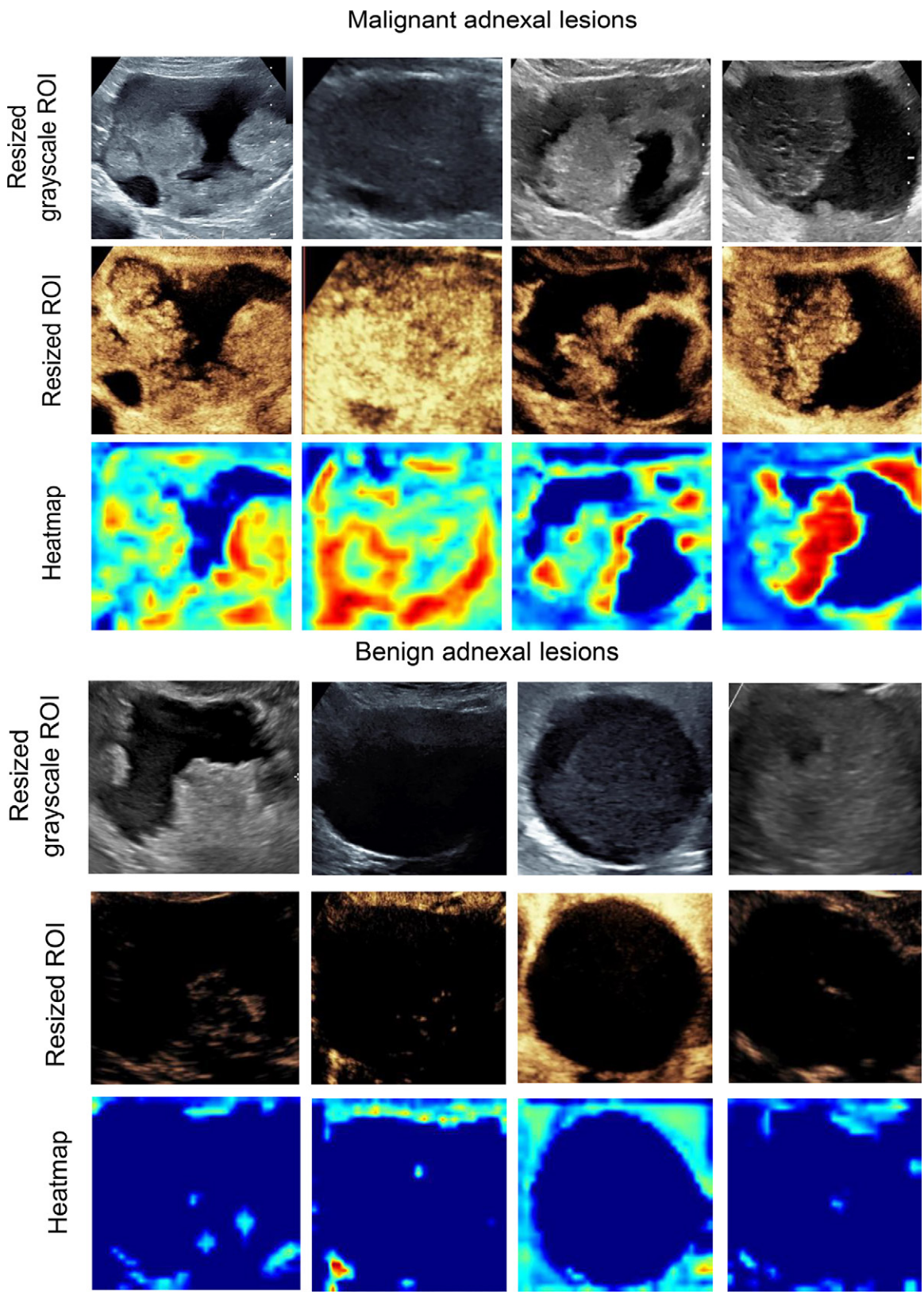

Figure 5: Examples of heatmaps generated by the Ovarian Cancer Network model for discrimination between malignant ovarian lesions and benign ovarian lesions. The first, second, and third rows in each section display the original B-mode US, contrast-enhanced US, and the corresponding heatmap, respectively. In the heatmaps, the color spectrum from red to blue indicates regions from high to low attention by the model, highlighting areas that most influenced its decision. Generally, for malignant lesions, the Ovarian Cancer Network focused on the tumor area, while for benign lesions, it focused on the lesion boundaries. ROI = region of interest.

Table 4: Details of Misclassified Cases by the Ovarian Cancer Network in the External Testing Set

Case ID	Age	Pathologic Result	US System	Lesion Type	Enhancement Pattern		
					Enhancement Time	Enhancement Intensity	Dynamic Change of Enhancement
$OCNet_{manual}$							
2-0-045	36	Infected endometrioma	EPIQ 7, Philips Healthcare	Solid	Early enhancement	Hyperenhancement	Hyperenhancement to hypoenhancement
2-0-046	31	Mature teratoma	EPIQ 7, Philips Healthcare	Multilocular cyst with solid component	Early enhancement	Isoenhancement	Hyperenhancement to hypoenhancement
2-0-094	55	Mature teratoma (struma ovarii)	LOGIQ E9, GE HealthCare	Solid	Late enhancement	Hypoenhancement	Hyperenhancement to hypoenhancement
2-0-099	48	Infected endometrioma	LOGIQ E9, GE HealthCare	Multilocular cyst with solid component	Synchronous enhancement	Isoenhancement	Isoenhancement to isoenhancement
2-1-001	35	Serous cystadenocarcinoma	EPIQ 7, Philips Healthcare	Multilocular cyst with solid component	Synchronous enhancement	Hypoenhancement	Hyperenhancement to hypoenhancement
2-1-032	18	Germ cell tumor	EPIQ 7, Philips Healthcare	Solid	Synchronous enhancement	Isoenhancement	Hyperenhancement to hypoenhancement
2-1-060	60	Mucinous borderline tumor	LOGIQ E9, GE HealthCare	Multilocular cyst without solid component	Late enhancement	Hypoenhancement	Hypoenhancement to hypoenhancement
$OCNet_{automated}$							
2-0-045	36	Infected endometrioma	EPIQ 7, Philips Healthcare	Solid	Early enhancement	Hyperenhancement	Hyperenhancement to hypoenhancement
2-0-094	55	Mature teratoma (struma ovarii)	LOGIQ E9, GE HealthCare	Solid	Late enhancement	Hypoenhancement	Hyperenhancement to hypoenhancement
2-0-099	48	Infected endometrioma	LOGIQ E9, GE HealthCare	Multilocular cyst with solid component	Synchronous enhancement	Isoenhancement	Isoenhancement to isoenhancement
2-0-087	52	Mature teratoma	LOGIQ E9, GE HealthCare	Unilocular cyst without solid component	Late enhancement	Hypoenhancement	Hypoenhancement to hypoenhancement
2-0-101	56	Serous cystadenoma	LOGIQ E9, GE HealthCare	Multilocular cyst with solid component	Late enhancement	Hypoenhancement	Hypoenhancement to hypoenhancement
2-0-104	31	Mucinous cystadenoma	LOGIQ E9, GE HealthCare	Multilocular cyst with solid component	Late enhancement	Hypoenhancement	Hypoenhancement to hypoenhancement
2-1-001	35	Serous cystadenocarcinoma	EPIQ 7, Philips Healthcare	Multilocular cyst with solid component	Synchronous enhancement	Hypoenhancement	Hyperenhancement to hypoenhancement
2-1-030	64	Mucinous borderline tumor	EPIQ 7, Philips Healthcare	Multilocular cyst with solid component	Synchronous enhancement	Isoenhancement	Isoenhancement to isoenhancement
2-1-032	18	Germ cell tumor	EPIQ 7, Philips Healthcare	Solid	Synchronous enhancement	Isoenhancement	Hyperenhancement to hypoenhancement

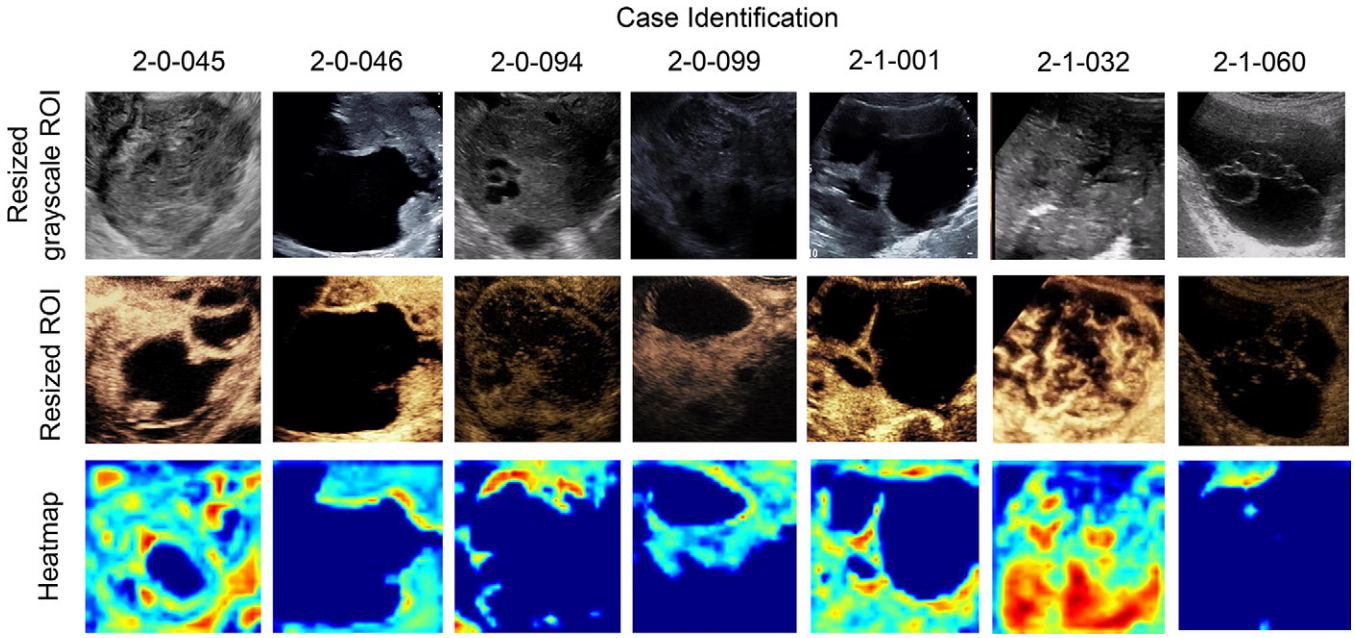

Figure 6: Heatmap visualization shows the misclassified seven cases by the Ovarian Cancer Network$_{manual}$ model. The first, second, and third rows display the original B-mode US image, contrast-enhanced US image, and the associated classification heatmap. The heatmap uses a color gradient, where red hues denote regions of highest model activation and blue hues indicate areas of lower attention. ROI = region of interest.

upgrade the O-RADS US score. Users should be aware that heatmaps that do not match the model's predictions may suggest mistakes and should be interpreted with caution. A self-supervision mechanism has been established to prevent overreliance and alert fatigue, by which the system occasionally presents deliberately incorrect outputs—roughly once a week—and if a user accepts these results, an alert is generated, promoting ongoing critical assessment of the AI assistance.

This study had limitations. First, as a retrospective analysis, our study revealed a higher prevalence of malignancy compared with prior studies (27,29), most likely due to selection bias in real-world data. Many adnexal lesions were referred from local hospitals to our specialized centers, resulting in more complex and malignant cases. Additionally, the use of surgical resection as the reference standard may have skewed results toward high-risk lesions, increasing the number of malignant cases. Second, the preprocessing of dynamic contrast-enhanced images still requires improvement. To address the issue of labor cost for manual extraction, we have incorporated an automated AI-driven framework for CEUS key-frame extraction. Yet the accuracy of the current automated AI-driven framework still needs to be enhanced. One potential reason for this limitation is that the AI model's ability to generate time-intensity curves may not achieve the same level of precision as manually generated time-intensity curves. Third, in the current study, we could not conduct a more in-depth analysis of the impact of various CEUS enhancement patterns on the model due to limited sample size. Finally, the 63-lesion external testing set was underpowered.

In conclusion, this study demonstrates that the proposed OCNet models can serve as a low-cost, easily accessible, and accurate diagnostic tool for adnexal lesions. The OCNet model integrated CEUS images for the first time and enables expert-level distinctions for adnexal lesions. With the assistance of the OCNet model, false-positive rates were significantly reduced without sacrificing high sensitivity. Our results indicated that the fusion of the OCNet model with radiologists' knowledge may enhance diagnostic accuracy, ultimately leading to better patient outcomes for those with ovarian cancer. Future prospective validation in prevalence-matched cohorts is needed to verify the generalizability and clinical value of the AI models.

Author affiliations:

[1] Department of Ultrasound, The Third Affiliated Hospital of Sun Yat-Sen University, 600 Tianhe Road, Guangzhou 510630, PR China

[2] School of Computer Science and Engineering, Sun Yat-Sen University, Guangzhou, PR China

[3] Department of Ultrasound, Central Hospital of Wuhan, Tongji Medical College, Huazhong University of Science and Technology, Wuhan, PR China

[4] Department of Ultrasound, Children's Hospital of Shanxi (Women's Health Center of Shanxi), Taiyuan, PR China

[5] Ultrasound Diagnosis Center, Shaanxi Provincial People's Hospital, Xian, PR China

[6] Department of Ultrasound, The Fifth People's Hospital of Chengdu, Chengdu, PR China

[7] Department of Ultrasound, Huizhou Central People's Hospital, Huizhou, PR China

[8] Department of Ultrasound, Henan Provincial People's Hospital, Zhengzhou, PR China

[9] Department of Ultrasound Medicine, The First Affiliated Hospital of Guangxi Medical University, Nanning, PR China

[10] Department of Ultrasound, The Third Hospital of BaoGang Group, The Maternity Hospital of Bao Tou, Baotou, PR China

[11] Department of Gynecology, The Third Affiliated Hospital of Sun Yat-Sen University, Guangzhou, PR China

[12] Department of Ultrasound, Nanchong Central Hospital, Nanchong, PR China

[13] Department of Ultrasound, Chengdu's First People's Hospital, Chengdu, PR China

[14] Department of Ultrasound, Renmin Hospital of Wuhan University, Wuhan, PR China

[15] Department of Ultrasound, The First Affiliated Hospital of Nanchang University, Nanchang, PR China

[16] Department of Ultrasound, The First Affiliated Hospital of Guangxi University of Chinese Medicine, Nanning, PR China

Received November 21, 2024; revision requested January 13, 2025; revision received September 30; accepted October 16.

Address correspondence to: X.Z. (email: zhxl@mail.sysu.edu.cn).

Supplemental material: Supplemental material is available at *Radiology: Artificial Intelligence* online.

Funding: Supported by grants from the National Natural Science Foundation of China (no. 82202191), the Guangzhou Basic and Applied Basic Research Foundation (no. 2024A04J4786), Science and Technology Projects of Guangzhou (no. 2023A03J0217), GuangDong Basic and Applied Basic Research Foundation (no. 2023A1515220008), and Natural Science Foundation of Guangdong Province, China (2022A1515012027). The funders had no influence on study design, data collection and analysis, decision to publish, or preparation of the manuscript.

Author contributions: Guarantors of integrity of entire study, **M.W., H.Y., Y.C., T. Liang, X.S., L.X., X.M., J.G., Yaping Wang, Q.Z., J.L., P.C., J.H., X.Z.**; study concepts/study design or data acquisition or data analysis/interpretation, all authors; manuscript drafting or manuscript revision for important intellectual content, all authors; approval of final version of submitted manuscript, all authors; agrees to ensure any questions related to the work are appropriately resolved, all authors; literature research, **M.W., H.Y., M.Z., E.Q., X.S., L.X., X.M., M.S., J.L., J.H.**; clinical studies, **M.W., H.Y., Y.C., M.Z., E.Q., X.S., R.Z., M.L., L.X., H.W., Ruili Wang, T. Liu, X.M., M.S., J.G., S.C., Yaping Wang, Q.Z., J.L., P.C.**; experimental studies, **H.Y., X.S., R.Z., L.X., X.M., Ying Wang, J.L., Ruixuan Wang, J.H.**; statistical analysis, **M.W., H.Y., S.W., X.S., L.X., X.M., Yaping Wang, J.L., Ruixuan Wang, J.H.**; and manuscript editing, **H.Y., T. Liang, M.Z., X.S., L.X., X.M., J.L., Ruixuan Wang, J.H., X.Z.**

Disclosures of conflicts of interest: **M.W.** No relevant relationships. **H.Y.** No relevant relationships. **Y.C.** No relevant relationships. **S.W.** No relevant relationships. **T. Liang** No relevant relationships. **M.Z.** No relevant relationships. **E.Q.** No relevant relationships. **X.S.** No relevant relationships. **R.Z.** No relevant relationships. **M.L.** No relevant relationships. **L.X.** No relevant relationships. **H.W.** No relevant relationships. **Ruili Wang** No relevant relationships. **T. Liu** No relevant relationships. **X.M.** No relevant relationships. **M.S.** No relevant relationships. **Ying Wang** No relevant relationships. **J.G.** No relevant relationships. **S.C.** No relevant relationships. **Yaping Wang** No relevant relationships. **Q.Z.** No relevant relationships. **J.L.** No relevant relationships. **P.C.** No relevant relationships. **Ruixuan Wang** No relevant relationships. **J.H.** No relevant relationships. **X.Z.** No relevant relationships.

References

1. Bray F, Laversanne M, Sung H, et al. Global cancer statistics 2022: GLOBOCAN estimates of incidence and mortality worldwide for 36 cancers in 185 countries. CA Cancer J Clin 2024;74(3):229–263.
2. Siegel RL, Giaquinto AN, Jemal A. Cancer statistics, 2024. CA Cancer J Clin 2024;74(1):12–49.
3. Xiao Y, Bi M, Guo H, et al. Multi-omics approaches for biomarker discovery in early ovarian cancer diagnosis. EBioMedicine 2022;79:104001.
4. Adjei NN, Haas AM, Sun CC, et al. Cost of ovarian cancer by the phase of care in the United States. Am J Obstet Gynecol 2025;232(2):204.e1–204.e13.
5. Moruzzi MC, Bolomini G, Esposito R, et al. Diagnostic performance of ultrasound in assessing the extension of disease in advanced ovarian cancer. Am J Obstet Gynecol 2022;227(4):601.e1–601.e20.
6. Suh-Burgmann EJ, Hung YY, Schmittdiel JA. Ovarian cancer risk among older patients with stable adnexal masses. Am J Obstet Gynecol 2024;231(4):440.e1–440.e7.
7. Zeng H, Zheng R, Guo Y, et al. Cancer survival in China, 2003-2005: a population-based study. Int J Cancer 2015;136(8):1921–1930.
8. McMullen M, Karakasis K, Rottapel R, et al. Advances in ovarian cancer, from biology to treatment. Nat Cancer 2021;2(1):6–8.
9. Sadowski EA, Rockall A, Thomassin-Naggara I, et al. Adnexal Lesion Imaging: Past, Present, and Future. Radiology 2023;307(5):e223281.
10. Piovano E, Cavallero C, Fuso L, et al. Diagnostic accuracy and cost-effectiveness of different strategies to triage women with adnexal masses: a prospective study. Ultrasound Obstet Gynecol 2017;50(3):395–403.
11. Campbell S, Gentry-Maharaj A. The role of transvaginal ultrasound in screening for ovarian cancer. Climacteric 2018;21(3):221–226.
12. Strachowski LM, Jha P, Phillips CH, et al. O-RADS US v2022: An Update from the American College of Radiology's Ovarian-Adnexal Reporting and Data System US Committee. Radiology 2023;308(3):e230685.
13. Wu M, Zhang M, Cao J, et al. Predictive accuracy and reproducibility of the O-RADS US scoring system among sonologists with different training levels. Arch Gynecol Obstet 2023;308(2):631–637.
14. Vara J, Manzour N, Chacón E, et al. Ovarian Adnexal Reporting Data System (O-RADS) for Classifying Adnexal Masses: A Systematic Review and Meta-Analysis. Cancers (Basel) 2022;14(13):3151.
15. Lee S, Lee JE, Hwang JA, et al. O-RADS US: A Systematic Review and Meta-Analysis of Category-specific Malignancy Rates. Radiology 2023;308(2):e223269.
16. Yuan K, Huang YJ, Mao MY, et al. Contrast-enhanced US to Improve Diagnostic Performance of O-RADS US Risk Stratification System for Malignancy. Radiology 2023;308(2):e223003.
17. Xu J, Huang Z, Zeng J, et al. Value of Contrast-Enhanced Ultrasound Parameters in the Evaluation of Adnexal Masses with Ovarian-Adnexal Reporting and Data System Ultrasound. Ultrasound Med Biol 2023;49(7):1527–1534.
18. Wu M, Zhang M, Qu E, et al. A modified CEUS risk stratification model for adnexal masses with solid components: prospective multicenter study and risk adjustment. Eur Radiol 2024;34(9):5978–5988.
19. Wu M, Wang Y, Su M, et al. Integrating Contrast-enhanced US to O-RADS US for Classification of Adnexal Lesions with Solid Components: Time-intensity Curve Analysis versus Visual Assessment. Radiol Imaging Cancer 2024;6(6):e240024.
20. Chen F, Han H, Wan P, et al. Do as Sonographers Think: Contrast-Enhanced Ultrasound for Thyroid Nodules Diagnosis via Microvascular Infiltrative Awareness. IEEE Trans Med Imaging 2024;43(11):3881–3894.
21. Landolfo C, Bourne T, Froyman W, et al. Benign descriptors and ADNEX in two-step strategy to estimate risk of malignancy in ovarian tumors: retrospective validation in IOTA5 multicenter cohort. Ultrasound Obstet Gynecol 2023;61(2):231–242.
22. Van Calster B, Van Hoorde K, Valentin L, et al; International Ovarian Tumour Analysis Group. Evaluating the risk of ovarian cancer before surgery using the ADNEX model to differentiate between benign, borderline, early and advanced stage invasive, and secondary metastatic tumours: prospective multicentre diagnostic study. BMJ 2014;349:g5920.
23. Moro F, Vagni M, Tran HE, et al. Radiomics analysis of ultrasound images to discriminate between benign and malignant adnexal masses with solid ultrasound morphology. Ultrasound Obstet Gynecol 2025;65(3):353–363.
24. Christiansen F, Epstein EL, Smedberg E, et al. Ultrasound image analysis using deep neural networks for discriminating between benign and malignant ovarian tumors: comparison with expert subjective assessment. Ultrasound Obstet Gynecol 2021;57(1):155–163.
25. Gao Y, Zeng S, Xu X, et al. Deep learning-enabled pelvic ultrasound images for accurate diagnosis of ovarian cancer in China: a retrospective, multicentre, diagnostic study. Lancet Digit Health 2022;4(3):e179–e187.
26. Miao K, Zhao N, Lv Q, et al. Prediction of benign and malignant ovarian tumors using Resnet34 on ultrasound images. J Obstet Gynaecol Res 2023;49(12):2910–2917.
27. Chen H, Yang BW, Qian L, et al. Deep Learning Prediction of Ovarian Malignancy at US Compared with O-RADS and Expert Assessment. Radiology 2022;304(1):106–113.
28. Xiang H, Xiao Y, Li F, et al. Development and validation of an interpretable model integrating multimodal information for improving ovarian cancer diagnosis. Nat Commun 2024;15(1):2681.
29. Barcroft JF, Linton-Reid K, Landolfo C, et al. Machine learning and radiomics for segmentation and classification of adnexal masses on ultrasound. NPJ Precis Oncol 2024;8(1):41.